



# Estimating Soil Organic Carbon using multitemporal PRISMA imaging spectroscopy data



Kathrin J. Ward <sup>a,\*</sup>, Saskia Foerster <sup>b</sup>, Sabine Chabrillat <sup>a,c</sup>

<sup>a</sup> German Research Centre for Geosciences (GFZ), Telegrafenberg, Potsdam, 14473, Germany

<sup>b</sup> German Environment Agency, Wörlitzer Platz 1, Dessau-Roßlau, 06844, Germany

<sup>c</sup> Leibniz Universität Hannover, Institute of Soil Science, Herrenhäuser Str. 2, Hannover, 30419, Germany

## ARTICLE INFO

Handling Editor: Budiman Minasny

**Keywords:**

Soil organic carbon  
PRISMA  
Hyperspectral  
Imaging spectroscopy  
Multitemporal  
SOC maps composite

## ABSTRACT

Soils are the largest terrestrial carbon pool and a valuable good that provides important ecosystem services. Since soils are threatened by degradation and in order to fight climate change the knowledge of the status quo especially of its soil organic carbon (SOC) content is required. A promising tool to map and monitor our soils are spaceborne imaging spectrometers which are able to produce up-to-date, inexpensive and spatially explicit maps. Especially the recent launch of new imaging spectroscopy sensors with a high signal-to-noise ratio opens up new possibilities. One of those is the combination of multitemporal spaceborne imaging spectroscopy data into SOC composite maps with a higher spatial coverage. This study explores different multitemporal combination workflows in order to support finding a best practice. To our knowledge for the first time, a spatially more complete SOC composite map was generated using four PRISMA images recorded over the same study site in northern Germany. Two different workflows of computation were compared: workflow one, creates a synthetical bare soil composite using averaged spectra as a basis for model development. Workflow two uses compositing after individual SOC modeling for each image. Within these workflows, different approaches were tested to estimate the SOC content, amongst them are a range of SOC spectral features and a two-step local PLSR which replaces the wet-chemistry SOC analyses for model calibration and validation by laboratory spectra and a large scale soil spectral library. Results show that the best method to produce a multitemporal composite SOC map based on imaging spectroscopy data was workflow two: the SOC maps composite, using the SOC spectral feature approach ( $R^2 = 0.83$ , RPD = 2.42). While workflow two and the traditional PLSR approach was more robust for all input dates ( $R^2 = 0.79$ , RPD = 2.21). Best results of the single images reached  $R^2$  values of 0.76–0.91 and RPD values ranging between 2.06–3.42. Three of the tested SOC spectral features provided accuracies comparable to the modeling approaches. These results are promising regarding the improvement of the spatial coverage and the refinement of the mapping and monitoring of SOC and other soil parameters. Further investigations in this direction are needed as they are precursors of what will be feasible by upcoming operational imaging spectroscopy missions with increased availability.

## 1. Introduction

The soils below our feet are the largest terrestrial organic carbon pool (Minasny et al., 2017; Soussana et al., 2019). They do not only provide important ecosystem services (e.g. food security) but they can potentially help to combat climate change, since a small increase of the soil organic carbon (SOC) stocks could lead to a reduced net flux of CO<sub>2</sub> towards the atmosphere (Vaudour et al., 2019). To support carbon sequestration the 4 per 1000 - soils for food security and climate initiative (4p1000) was launched (COP21 in 2015). To compensate for anthropogenic greenhouse gases (GHG) it aims at increasing the global SOC stocks by 0.4% per year which is approximately the ratio

of the global anthropogenic carbon emissions (8.1 Gt/year) and the total SOC stock (2400 Gt) (Minasny et al., 2017; Soussana et al., 2019). Also global policies such as the sustainable development goals (SDGs) of the United Nations regard SOC as the most relevant soil property in terms of climate regulations (Tóth et al., 2018). Additionally, there are the land neutrality target of the UN Framework Convention on Climate Change—Intergovernmental Panel on Climate Change (UNFCCC-IPCC) and the “Caring for Soil” mission of the European Commission (Tziolas et al., 2021). This shows the urgent necessity to map and monitor the SOC content especially in top soils (Vaudour et al., 2019). However, most currently available high-resolution SOC

\* Corresponding author.

E-mail address: [kathrin.ward@gfz-potsdam.de](mailto:kathrin.ward@gfz-potsdam.de) (K.J. Ward).

maps are static and based on outdated point data (Minasny et al., 2017; Tziolas et al., 2021). Therefore, alternative methods are needed that are capable to produce maps which are up-to-date, inexpensive and spatially accurate (Chabriat et al., 2019).

One alternative is to use soil spectroscopy, which uses the visible, near to shortwave infrared (VNIR-SWIR) part of the electromagnetic spectrum to estimate spectrally active soil properties (Chabriat et al., 2019). SOC is composed of a mixture of biochemical materials, e.g. chlorophyll, cellulose, starch, oil, pectin, lignin and humic acids (Beyer et al., 2001) which absorb radiation in the VNIR-SWIR range (Ben-Dor et al., 1997). It shows strong interactions in the visible (VIS) part of the spectrum which lead to a general flattening of the reflectance curve in this part. This is caused by the decomposition of chlorophyll pigments that originally led to a wide spectral absorption feature around 664 nm (Ben-Dor et al., 1997; He et al., 2009). Additionally, there are strong and narrow absorption features of SOC in the SWIR between 2100–2300 nm which are pronounced in lignite-rich soils (Ben-Dor et al., 1997; He et al., 2009; Viscarra Rossel and Behrens, 2010). Since soils are a mixture of different materials they have weak, broad and superimposing absorption features. To estimate a certain soil property like SOC, most studies use partial least squares regression (PLSR), Random Forest (RF) or other machine learning techniques as they cope well with the large number of highly collinear predictor variables (Vaudour et al., 2022).

Under laboratory conditions soil spectroscopy is a well established method (Nocita et al., 2015) and also imaging spectroscopy from airborne platforms has already been widely used for local studies with good accuracies (Ben-Dor et al., 2009; Chabriat et al., 2019). The first pioneering spaceborne imaging spectroscopy missions were NASA's Hyperion (November 2000 - March 2017) (Folkman et al., 2001; Middleton et al., 2017) and ESA's Compact High-Resolution Imaging Spectrometer (CHRIS) (October 22nd 2001 - today) (Barnsley et al., 2004). These pioneering missions have a lower signal-to-noise ratio and therefore studies estimating SOC show medium accuracy (Gomez et al., 2008). Just recently they were followed by the second generation of spaceborne sensors with higher signal-to-noise ratios. These are e.g. the Chinese GaoFen-5 Advanced Hyperspectral Imager (AHSI, launched 2018, data not freely available) (Liu et al., 2019), the Italian PRecursore IperSpettrale della Missione Applicativa (PRISMA, launched 2019) (Cogliati et al., 2021) and the German Environmental Mapping and Analysis Program (EnMAP, launched 2022) (Storch et al., 2023). Additionally there are three sensors deployed on the International Space Station (ISS): the German DLR Earth Sensing Imaging Spectrometer (DESIS, launched 2018) covering only the spectral range between 400–1000 nm (Alonso et al., 2019), the Japanese Hyperspectral Imager Suite (HISUI, launched 2019, data not freely available) (Urai et al., 2021) and NASA's Earth Surface Mineral Dust Source Investigation (EMIT, launched 2022) (Green et al., 2023) which is on a fixed acquisition plan. Further planned third generation satellite sensor missions will acquire operationally and globally unlike the current second generation sensors. These missions are the ESA's Copernicus Hyperspectral Imaging Mission for the Environment (CHIME) (Nieke and Rast, 2018) and NASA's Surface Biology Geology (SBG) (Thompson et al., 2020; Cawse-Nicholson et al., 2021) and they are expected after 2028.

To date few studies have been published using spaceborne imaging spectroscopy data of the second generation for the quantification and mapping of SOC. They have been based on either PRISMA or the Chinese satellites GaoFen-5 and ZY1-02D (the data of GaoFen-5 and ZY1-02D are not freely available). Only one study used multitemporal PRISMA data but without combining them into one soil property map (Mzid et al., 2022). An overview is provided in Table 1.

Imaging spectroscopy from air- and spaceborne platforms is challenged by different factors which are subject of current research, e.g. soil surface conditions (mainly moisture content, roughness and crusts), mixing with green or dry vegetation cover (Ben-Dor et al., 2008; Chabriat et al., 2019). When going from local to regional or larger

scale, soils will be more inhomogeneous which increases the variability of the soil property and could also lead to non-linear relationships between soil property and spectra making model calibration more difficult (Stenberg et al., 2010; Nocita et al., 2014; Stevens et al., 2013). Another issue is the availability of a database of local ground reference soil samples. Updating this database is time and cost intensive especially due wet-chemistry analyses. Additionally, in the temporal climate zone soils are typically bare in spring and late summer but not all fields are bare at the same point in time. Due to crop rotation the location of bare fields differs in between years and this influences the number of match ups between bare soil pixel and the local soil database. To overcome the challenge of temporally bare soils, it is beneficial to combine multitemporal images from different dates and a few years into a temporal composite. This was already done using multitemporal multispectral data, such as Sentinel-2 (Castaldi et al., 2023; Vaudour et al., 2021; Zepp et al., 2021). So far, multitemporal spaceborne imaging spectroscopy data has never been used for soil compositing. Until recently, high quality imaging spectroscopy data has only been available through airborne acquisitions. Since they are cost and time expensive as well as limited to a smaller area, they can rarely be conducted at regular time intervals. One exception is the study by Gerighausen et al. (2012) who successfully used airborne imaging spectroscopy acquisitions for SOC and clay estimation of three different years and found only few overlapping bare soil areas when comparing the three images.

The first aim of this study is to further investigate and prove the potential of the latest spaceborne imaging spectroscopy missions using data of the PRISMA sensor. Imaging spectroscopy data of four images acquired over the same study site at different dates within two years was utilized to estimate the SOC content. For model calibration and validation a database of local ground reference soil samples as well as the European LUCAS Soil database were used. In order to model the link between spectra and SOC, a range of established techniques was applied, such as different spectral features, machine learning and regression techniques, and additionally the performance of a two-step local PLSR approach (Ward et al., 2020a) was tested. A second aim was to investigate different workflows for creating one SOC map composite out of the four PRISMA images. Therefore, workflow one was similar to the established workflow which is already applied to multitemporal multispectral archives. In this workflow bare soil compositing was done first, followed by SOC prediction. This workflow was compared to a new workflow where SOC was predicted on each individual time-frame before spatially compositing all SOC property maps. To our knowledge the temporal composite has not been computed previously based on spaceborne imaging spectroscopy data for soil property estimation and it opens up new possibilities for creating more complete SOC maps.

## 2. Data and methods

### 2.1. Data

**Study site:** The study site is situated in the North-East of Germany centered around a town called Demmin. It is located in the federal state of Mecklenburg-Western Pomerania and is included in the observatory Northeastern German Lowland. This is a part of the TERrestrial ENvironmental Observatories (TERENO) being a long term terrestrial environmental monitoring site initiated by the German Helmholtz Association (Zacharias et al., 2011). Additionally, the site is associated with the Durable Environmental Multidisciplinary Monitoring Information Network which is the German JECAM site DEMMIN operated by the German Aerospace Center (Deutsches Zentrum fuer Luft- und Raumfahrt, DLR) and the German Research Centre for Geosciences (GFZ) Potsdam (Spengler et al., 2018).

The area was formed during the Pleistocene (Weichselian Glaciation) and its undulated terrain is shaped by periodic glacial processes. It belongs to the young morainic soil landscape of northern Germany.

**Table 1**

Overview of studies using spaceborne imaging spectroscopy sensors to predict the SOC or SOM content. RMSE in g/kg; n = number of samples; min/mean/max refers to the measured SOC content; RF = Random Forest; OK Ordinary Kriging; OLS = ordinary least-squares regression; BPNN = back-propagation neural network; RFE Recursive Feature Elimination; CNN = convolutional neural network; TI = topography input variable; ELM = extreme learning machine; RR = ridge regression.

Sensor	Method	R <sup>2</sup>	RPD	RPIQ	RMSE	n	min	mean	max	Site	Reference
PRISMA	RF OK	0.69	–	2.56	3.4	107	9.7	30.9	44	Marocco	Gasm et al. (2022)
PRISMA	Cubist	0.85	2.43	3.51	1.7	43/18	1.8/9.6	9.5/14.4	20.9/18.0	Italy	Mzid et al. (2022)
PRISMA	Cubist	0.76	2.06	3.31	1.22	30	11	38	86	Greece	Angelopoulou et al. (2023)
PRISMA	OLS	0.64	–	–	–	100	6.8	18.7	93.4	Italy	Salani et al. (2023)
GF-5	BPNN	0.83	2.05	–	2.89	315	2.47	22.46	45.84	China	Meng et al. (2020)
GF-5	RFE-RF	0.84	–	1.71	3.36	166	26.1	40.81	56.3	China	Meng et al. (2021)
GF-5	RFE-RF	0.76	–	2.28	3.16	278	2.46	22.46	45.84	China	Bao et al. (2021)
GF-5	CNN+TI	0.86	–	1.91	2.49	796	2.46	21.19	45.83	China	Meng et al. (2022)
ZY1-02D	RF+ELM+GPR+RR	0.83	2.85	–	1.95	67	10.6	24.16	39.6	China	Wu et al. (2023)

The main soil types of the study site within the coverage of the satellite images are Gleysols in the North, Regosols/Arenosols/Podzoluvisols/Cambisols in the center and Luvisols in the South. Alongside the riverbeds there are eutric Histosols (BGR, 2013). Soil collection was performed in areas with the following topsoil types: sandy loams (sl) in the western part, loamy sands (ls) in the eastern part and a few samples on peatland soils (BGR, 2007). The sampling areas generally show a high variability in SOC content at small scale and the large crop fields are well suited for remote sensing studies.

**Soil samples:** A total of 183 top-soil samples (0–10 cm depth) were collected within the study site in October 2013, 2016 and 2017. The SOC content is assumed to be rather constant over the investigated period of time, as e.g. De Rosa et al. (2024) report a SOC change for agricultural European soils between the years 2009 and 2018 of  $-0.04 \pm 0.01$  g/kg per year, based on revisited points in the LUCAS Soil database. These samples were used for model and spectral feature generation and assessment. The samples were collected in a way that they are well representing the sampled fields and cover the range of SOC values in the area. Within a radius of 5 m around the central location five sub-samples were collected and mixed. Subsequently, they were dried, gently crushed and sieved (<2 mm). For all samples the SOC content was measured by dry combustion using a VarioMax CN Analyzer (Elementar Analysensysteme GmbH, Germany). For a set of 48 samples spectral absorbance was measured with a FOSS XDS Rapid Content Analyzer in the REQUASUD network laboratories of the Province of Liege (Genot et al., 2011). The XDS data range from 400.0–2499.5 nm and have a spectral resolution of 0.5 nm, resulting in 4200 wavelengths. The remaining 135 samples have no additional spectral laboratory measurements included.

Additionally, the European Land Use/Cover Area Frame Survey (LUCAS) topsoil database was used which is provided by EUROSTAT together with the European Commission's Directories-General for Environment and the Joint Research Centre at Ispra, Italy (Orgiazzi et al., 2018; Toth et al., 2013). The data collected for the survey in 2009 was applied and a subset of approximately 8000 samples of the database consisting of samples collected on agricultural areas was used. The samples are top-soil samples (0–20 cm depth) and were dried at 40 °C, crushed and sieved (<2 mm). The SOC content was also measured by dry combustion using a VarioMax CN Analyzer (Elementar Analysensysteme GmbH, Germany). The SOC content in the LUCAS agricultural subset spans from 0–194 g/kg and is highly right skewed including few high values (median 14.4 g/kg). The LUCAS soil database includes spectral absorbance measurements acquired using a FOSS XDS Rapid Content Analyzer (FOSS NIR Systems Inc., Laurel, MD, USA). They have the same spectral range and resolution as the spectral measurements of the local soil samples (Toth et al., 2013).

**PRISMA images:** Four cloud-free scenes recorded over the study site were used as data basis of this study. They were downloaded from the archive of the data portal (<https://prisma.asi.it/>) in March 2022 using the improved L2D processor with high geometric and atmospheric corrections. The images are suitable as they have a low cloud cover

(<0.1%) and show a large proportion of bare soils in the agricultural areas. In the temperate climate zone bare soils are typically only visible at early spring and late summer. Three images were acquired in the year 2020 (07.08, 13.08., 22.09.) and one in 2021 (13.08.), see Fig. 1. The solar zenith angles of the images are 39, 40, 55 and 40°, and the viewing zenith angles are 6.2, 11.5, 4.4 and 1.2° (images (A) to (D)).

## 2.2. Methods

**Image pre-processing.** The imaging spectroscopy data acquired by the PRISMA satellite were unpacked and loaded into the EnMAP-Box which includes a PRISMA L2D reader that can directly load the \*.he5 format. After storing the images in a \*.bsq format they were spatially co-registered applying the local co-registration algorithm in the Python package AROSCS (Scheffler et al., 2017; Scheffler, 2017) and using a cloud free Sentinel-2 image from the same season as a reference. The first PRISMA image was spatially registered to the Sentinel-2 image while the other PRISMA images were co-registered to that first PRISMA image in order to align all pixel grids of the four PRISMA images.

For model generation image pixel values were extracted at the location of the soil samples using the bilinear extraction method which interpolates the values of the four nearest pixel cells (R function raster::extract Hijmans and van Etten, 2012).

The following spectral bands were removed due to being in the water vapor absorption ranges, noisy or in the overlapping region between the VNIR and SWIR detectors (rounded in nm): ≤456, 719–739, 760–770, 813, 951, 962, 973, 855–960, 1120–1163, 1251–1284, 1317–1534, 1765–2027 and ≥2350.

A Savitzky-Golay smoothing was applied using a second order polynomial and a window size of 13 bands (R function signal::sgolayfilt signal developers, 2014), based on visual comparison with laboratory spectra. In order to identify exposed soils, a bare soil mask was applied in R using the robust and proven spectral indices for bare soil discrimination from green and dry vegetation defined in EnSoMAP/HYSOMA (Chabrilat et al., 2011, 2016). For reasons of comparability the same thresholds were used for all images and were optimized in a grid search, testing different combinations of thresholds. To exclude pixels with green photosynthetically active vegetation, the normalized difference vegetation index (NDVI) was used with a threshold of <0.3. For residues and dry non-photosynthetically active vegetation, the normalized cellulose absorption index (nCAI) as defined and tested in Chabrilat et al. (2011, 2016) was used with a threshold of <0.014. To exclude pixels with moist soils, the normalized soil moisture index (NSMI) (Haubrock et al., 2008) was used with a threshold of <0.14. Furthermore, we removed pixels containing blooming algae in the Kummerower See (lake in south west of scene) by using a threshold of <0.02 for the mean reflectance in the range of 2200–2300 nm. This reflectance range and threshold were found empirically by comparing algae and soil spectra in the images.

$$NDVI = \frac{R_{802} - R_{660}}{R_{802} + R_{660}} \quad (1)$$

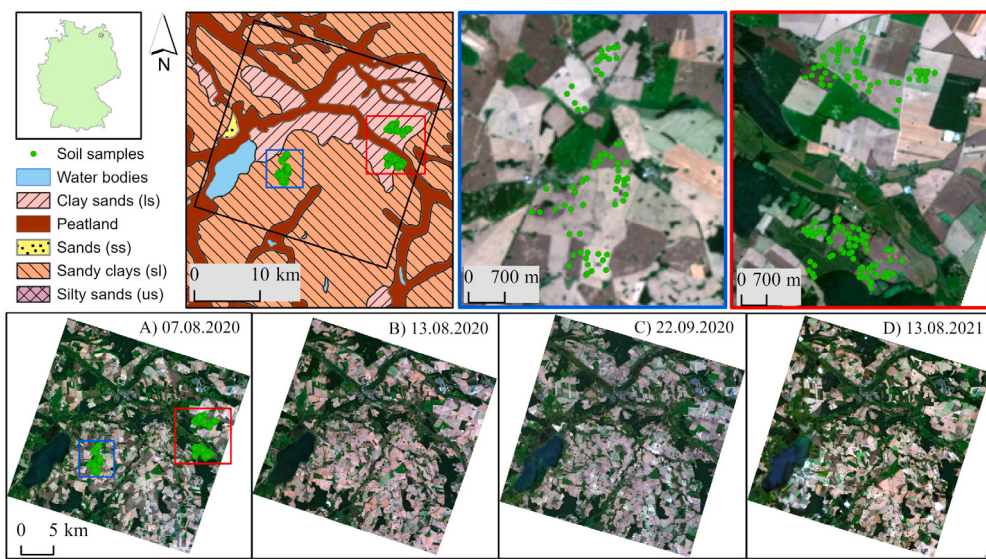


**Fig. 1.** Overview of the study site with top-soil types and soil samples (green dots). Four PRISMA images were used in this study and are shown as true-color RGB. The zoom into the study sites is based on the PRISMA image (A).

$$nCAI = \frac{0.5 * (R_{2036} + R_{2199}) - R_{2103}}{0.5 * (R_{2036} + R_{2199}) + R_{2103}} \quad (2)$$

$$NSMI = \frac{R_{1756} - R_{2119}}{R_{1756} + R_{2119}} \quad (3)$$

**Regression and machine learning approaches.** Four approaches were compared which are described in the following paragraphs and an overview is given in Fig. 2: (a) SOC spectral feature approach, (b) a two-step local PLSR approach, (c) and (d) traditional models which differ in their type of validation. For the approaches (b) and (c) the dataset was divided into the same calibration and validation subsets in order to have comparable results. Due to the design of approach (b) this fixed split was selected and also applied to approach (c) to estimate the amount of uncertainty added by approach (b). In approaches (a) and (d) a repeated random 5-fold cross validation was used for evaluation. For the modeling approaches (b)–(d) the first derivative was used as modeling input and calculated based on the smoothed absorbance spectra  $A = \log(1/\text{reflectance})$ . In approach (a) smoothed reflectance spectra were used. The measured SOC values of the ground reference samples, that were assigned to the corresponding image spectra, were often highly skewed and therefore transformed towards a normal distribution using the inverse.

(a) SOC spectral feature approach: A range of SOC indices or spectral features was tested for their applicability to this dataset (see Fig. 2(a)). In addition to the four SOC spectral features developed by Bartholomew et al. (2008) termed SOC1–4, three additional spectral features from the literature were tested: the feature named SOC5 in this study and introduced by Thaler et al. (2019); the SWIR/NIR named SOC6 (Frazier and Cheng, 1989); and a SOC7 spectral feature developed by Peón et al. (2017). The calculated spectral features were linked to the measured SOC values of the soil samples using a linear regression and evaluated by applying a repeated random 5-fold cross validation.

$$SOC1 = \frac{1}{\sum_{i=464}^{699} R_i} \quad (4)$$

$$SOC2 = \frac{1}{slope(R_{464:699})} \quad (5)$$

$$SOC3 = \frac{1}{area(R_{2053:2199})} \quad (6)$$

$$SOC4 = \frac{1}{slope(R_{2135:2199})} \quad (7)$$

$$SOC5 = \frac{R_{478}}{R_{546} * R_{660}} \quad (8)$$

$$SOC6 = \frac{R_{1606}}{R_{834}} \quad (9)$$

$$SOC7 = \frac{R_{998} - R_{679}}{R_{998} + R_{679}} \quad (10)$$

(b) two-step local PLSR approach: The local PLSR approach (Ward et al., 2020b) was developed based on Nocita et al. (2014) and Ward et al. (2019) and adapted to airborne data using a two-step approach by Castaldi et al. (2018) and Ward et al. (2020a). The benefit of this approach is that it can be used without knowing the SOC content of the local dataset measured by wet-chemistry. This information is replaced by SOC contents that are estimated based on laboratory spectra of the local samples and on a large scale soil spectral library which was the LUCAS Soil database in this study (Ward et al., 2020a) (first step with laboratory models). In a second step, these estimated SOC contents are used as the model's response variable together with the satellite spectra as predictors (spaceborne models). This method used a split of the dataset into calibration and validation subsets. The sampled fields were divided into calibration and validation fields to ensure independence and at the same time a similar variance for both subsets. Additionally, the calibration site was selected based on expert knowledge by choosing a large field with high variance representative for the area. Spectral laboratory measurements were performed for the calibration subset only.

(c) traditional models with cal/val: The traditional way of estimating the SOC content is to model the link of the pixel based imaging spectroscopy signal and the corresponding SOC content measured for a range of local soil samples. Model calibration and an independent validation were performed with the same split as described for approach (b).

(d) traditional models with cross validation: Furthermore, the same traditional approach was applied but with a repeated random 5-fold cross validation using measured SOC contents.

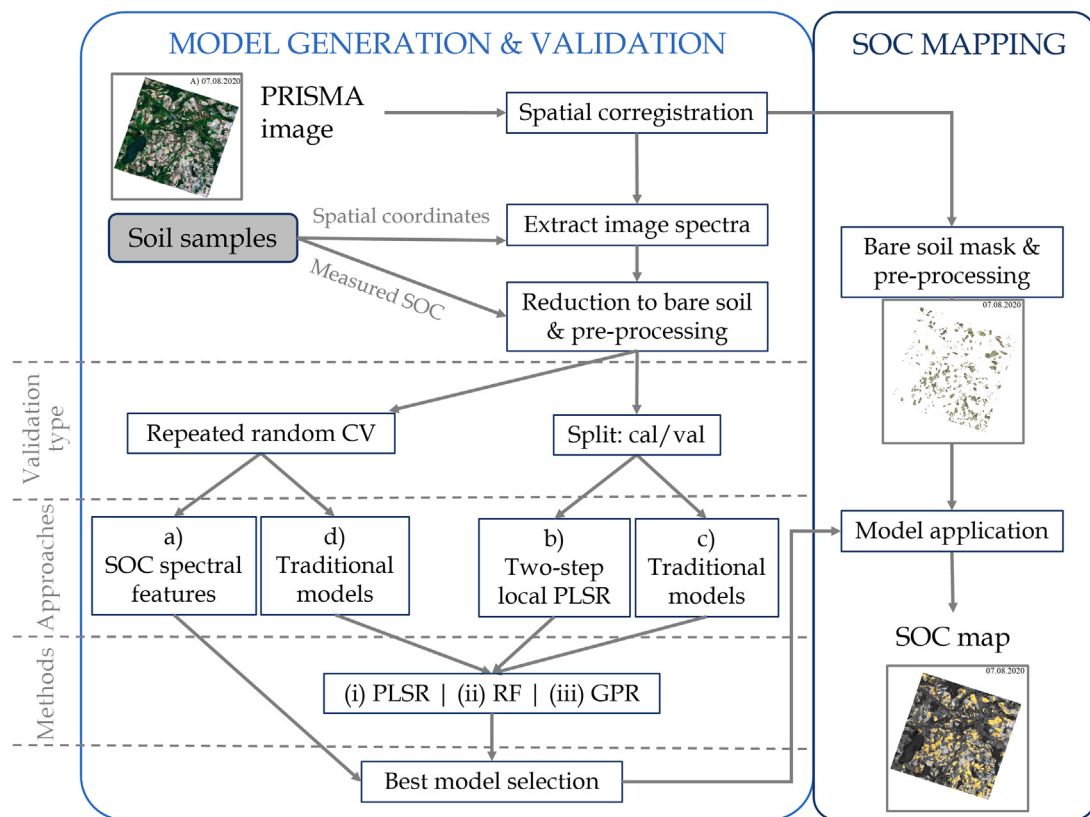


**Fig. 2.** Processing workflow showing model generation and SOC mapping for single images. CV = cross validation, cal/val = data split into calibration and validation subsets.

For each of the approaches (b)–(d) the three following multivariate modeling and machine learning methods were tested to find the ones most suitable for the datasets. An exception is the first step in the two-step local PLSR which always uses the PLSR. Approach (a) is a special case since it uses a linear regression to link the SOC index/spectral feature values with measured SOC contents.

(i) Partial least squares regression (PLSR) is among the most often used algorithms for SOC estimation from imaging spectroscopy data. It can cope well with the large number of highly redundant input variables as the PLSR combines data compression and regression. Successively, orthogonal factors are selected in order to maximize the covariance between the wavelengths as predictor and the SOC content as response variable (Martens and Naes, 1989; Viscarra Rossel and Behrens, 2010). The best number of these latent variables was selected by internal cross validation and minimizing the root mean squared error (RMSE). The `pls` function in R (R function `pls::pls` Lillard et al., 2021) was used.

(ii) Random forest (RF) using regression trees is also widely applied in this context. It consists of multiple trees and the individual tree outputs are averaged for a final prediction value (Breiman, 2001). RF can handle small datasets with a large number of predictor variables, it needs very little fine-tuning, is robust to noise and unimportant predictors and it does not overfit the results (Díaz-Uriarte and Alvarez de Andrés, 2006). The R function `randomForest` was applied (`randomForest::randomForest` Liaw and Wiener, 2002) and the number of variables randomly sampled as candidates at each split was selected as  $p/3$  with  $p$  = number of variables while number of trees was set to a sufficiently large number to allow for every input row to get predicted a few times.

(iii) Gaussian process regression (GPR) is a Bayesian approach which is a suitable algorithm for high-dimensional data and copes well with small datasets (Rasmussen, 2004). We used the gaussian radial basis kernel function ("rbfdot", R function `kernlab::gausspr` Karatzoglou

et al., 2022, 2004) and optimized the hyper-parameter in a grid search. The selected hyper-parameter values vary between 0.001–0.002 for the sigma parameter and 0.001–0.05 for the variance parameter.

*Multitemporal image generation and SOC mapping.* With the aim to generate a spatially more complete SOC map of a certain area, it is beneficial to combine multiple images acquired at different dates in time with varying bare soil areas depending e.g. on crop rotations. Multitemporal SOC maps were generated based on the pre-processed bare soil maps of all images. To increase processing speed, tiling (R function `terra::makeTiles`, Hijmans (2021)) and parallel computing on multiple cores were used. In order to find a best practice for SOC map generation based on multitemporal data, two different workflows of generating temporal composites were compared beginning at two different processing levels. An overview is given in Fig. 3.

For workflow one, referred to as the bare soil composite, all pre-processing steps including the bare soil masking and the extraction of pixel values at the locations of the soil samples were performed separately for each image. Afterwards, the extracted values of all four images were combined into one multitemporal spectral dataset by testing the mean and median pixel value for those pixels with bare soils in more than one image. Subsequently, the above mentioned spectral feature and modeling approaches for SOC estimation were developed on this synthetic multitemporal imaging spectroscopy dataset. It was computationally less expensive to find the best pre-processing set-up, train and validate the models based on the spectra extracted from the image and corresponding to the local reference samples. Only for map generation the whole image was pre-processed. In order to retrieve multitemporal SOC maps a synthetic multitemporal bare soil image was generated by merging all four bare soil maps and calculating the mean or median reflectance for pixels with bare soils in more than one of the images (Fig. 3 top). Subsequently, the multitemporal models and SOC spectral features were applied to all bare soil pixels of the synthetic image.

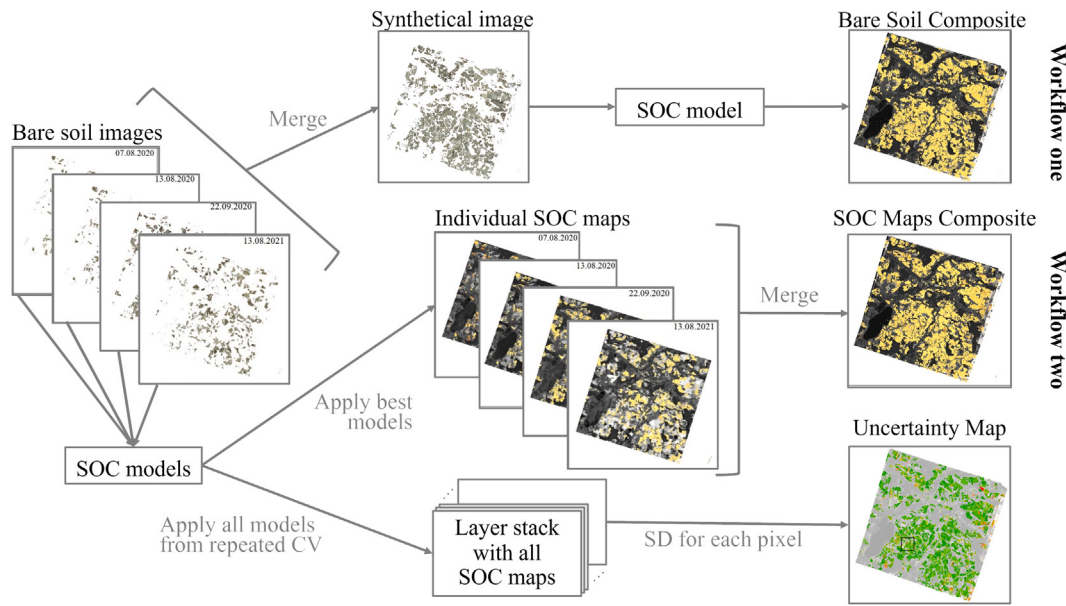


**Fig. 3.** Overview of multitemporal image processing workflows and uncertainty map generation. The two approaches for SOC mapping are the bare soil composite (workflow one; top) and the SOC maps composite (workflow two; middle).

Workflow two, referred to as the SOC maps composite, was based on the individual SOC maps generated for each of the images separately with their individual models. Models were developed for each image and for each of the four approaches described above (see Fig. 2a–d). Subsequently, these models were applied to all pre-processed and bare soil pixels of the respective image to generate individual SOC maps for the corresponding dates. To produce a temporal composite the single date SOC maps were merged. In order to derive a single SOC value per pixel the mean or median was used if more than one SOC value per pixel was available (Fig. 3 middle).

An uncertainty map (Fig. 3 bottom) was generated for the traditional approach (d) which was using a repeated random 5-fold cross validation. This cross validation was repeated 100 times which resulted in 100 models for the same image (A–D). All these models were applied to all bare soil pixels of the corresponding image. This was repeated for all four images (A–D) leading to 100 to 400 predicted SOC values per pixel, depending on the availability of bare soils. On this basis the standard deviation was calculated as a measure of uncertainty for the predictions.

**Model accuracy.** To asses the accuracies of the models we used the coefficient of determination ( $R^2$ ), the ratio of performance to deviation (RPD), the ratio of performance to interquartile range (RPIQ), the root mean squared error (RMSE) and the bias:

$$RMSE = \left( \sum_{i=1}^n \frac{(yp_i - yo_i)^2}{n} \right)^{1/2} \quad (11)$$

$$R^2 = 1 - \sum_{i=1}^n (yp_i - yo_i)^2 / \sum_{i=1}^n (yo_i - \bar{yo})^2 \quad (12)$$

$$RPD = \frac{sd(yo)}{RMSE} \quad (13)$$

$$RPIQ = \frac{IQ(yo)}{RMSE} \quad (14)$$

$$bias = \frac{1}{n} * \sum_{i=1}^n (yp_i - yo_i)^2 \quad (15)$$

with  $yo_i$  being the observed SOC value of sample i and  $yp_i$  being the predicted SOC value of sample i.  $yo$  is the mean of the observed SOC values, n is the number of samples, sd is the standard deviation and IQ is the interquartile range.

### 3. Results

The co-registration reduced initial shifts of up to 180 m to shifts up to 18 m which is at sub-pixel scale. Bare soil maps were generated of all four images. The percentage of bare soils within each image varied: it was 12% for image A (07.08.2020), 15.6% for image B (13.08.2020), 24.3% for image C (22.09.2020) and 14.4% for image D (13.08.2021). The absolute number of usable samples also differed for the images from 27 (image D) to 123 (image C) for the single images (for further details see Tables 2 & 3). It was dependent on the presence or absence of bare soil within the image pixels corresponding to the soil samples which was subject of change in between the different dates. The best methods for all approaches were either generated using PLSR or GPR.

For the multitemporal bare soil map, using median spectra proved to be better than using mean spectra. In Fig. 4(E) a high proportion of 37.9% of the total area shows exposed soils using the four images. Especially, in the image (C) acquired on 22nd September 2020 many fields were not covered by vegetation. The image acquired one year later (13.08.2021) adds to this as different fields showed bare soils due to management reasons such as crop rotation. Additionally, there are field that were bare in images (A) or (B) in August 2020 but not anymore in image (C) a month later. The spectral responses in between images for the same pixels were mainly similar for the three images recorded in 2020 with larger dissimilarities in the SWIR (see blue spectra in Fig. 5 as an example). Larger differences occurred for some pixels comparing the acquisitions from the years 2020 and 2021 (see pink spectra in Fig. 5 as an example). Within the used dataset, the maximum frequency of bare soil pixel per soil sampling location was three out of the four and this always included the three images acquired in 2020. For the approaches using the fixed split into calibration and validation, the percentage of samples falling into the calibration split varied between approximately 30% in images C–E to 60% in images A and B. Especially in image D the absolute number of calibration samples on bare soil pixels was very low (6 samples). The distribution of SOC contents differed for the images and was highly right skewed with very few high SOC values (Fig. 6). The very high SOC values with SOC

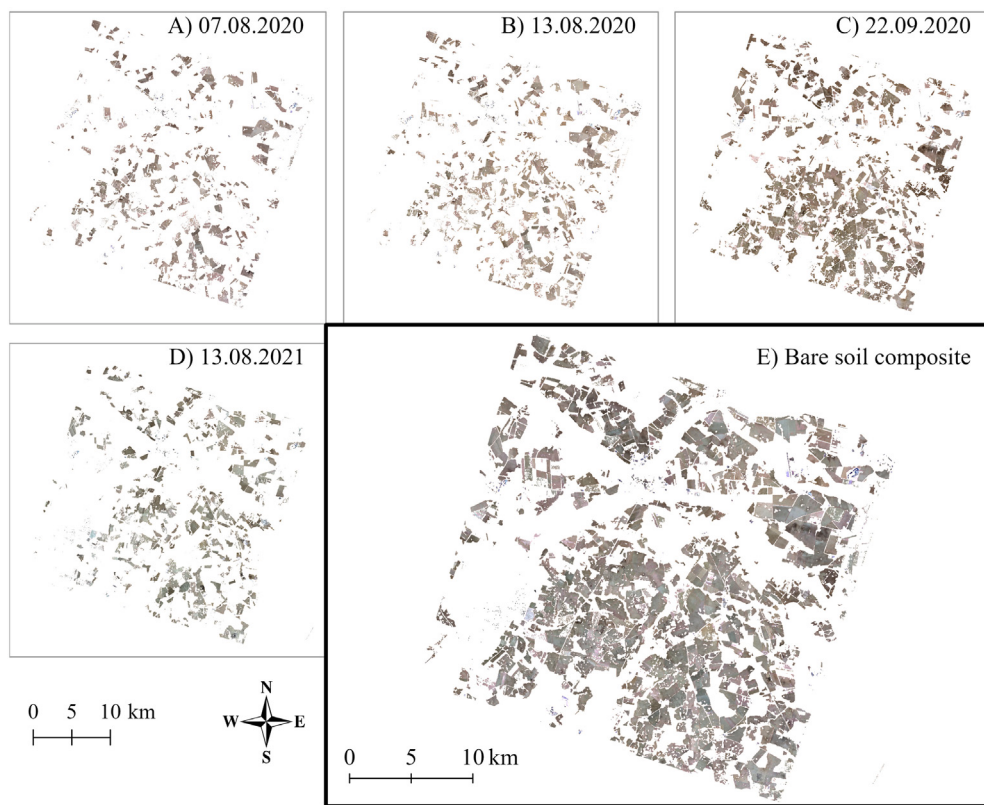


**Fig. 4.** True color RGB of the four PRISMA images (A–D) and the bare soil composite (E) showing bare soil pixels only. The bare soil composite is composed of the median spectra of all four PRISMA images.

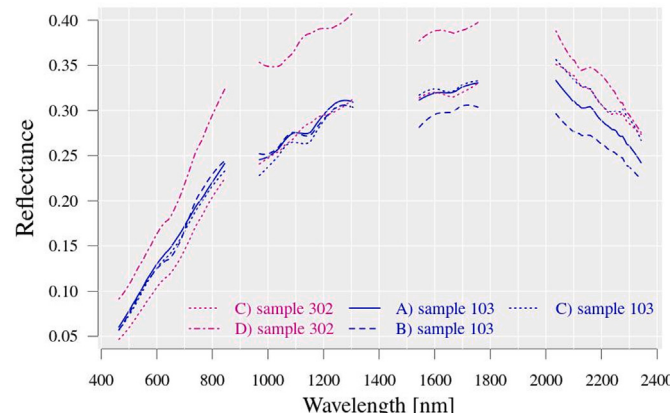


**Fig. 5.** Smoothed spectra at the location of two soil samples (302, 103) from two (C, D) resp. three PRISMA images (A–C). Sample 103 has a SOC value of 8.33 g/kg while sample 302 has a SOC value of 10.15 g/kg.

contents >60 g/kg always fell into the calibration split. Besides this, the distributions of calibration and validation subsets were similar. An exception is image D where the highest SOC contents were around 20 g/kg, indicating that no high SOC values were part of the dataset.

### 3.1. Single images and bare soil composite

For each of the four PRISMA images (A–D) and the synthetical multitemporal bare soil composite (workflow one, image E) the modeling results of approaches (a)–(d) are assessed and described in this subsection.

#### Approach (a) spectral feature approach

Seven spectral features were calculated and their performances are shown in Fig. 7. The range of results is produced by the repeated random cross validation. Regarding the best results, the RPD was >2 for SOC1, SOC2 and SOC5 and the two images from August 2020 (A, B), and >1.5 for image (C). For image (E) the bare soil composite and especially image (D) from August 2021 the accuracies were low. The images (C) and (E) showed a less linear relation between the spectral feature and the measured SOC content and therefore, benefited from using log(SOC).

In Fig. 8 the relation between SOC spectral feature and measured SOC content for the different images (A–C, E) is shown. In general the links between the images A and B were similar and so were the links of images C and E, with a steep gain in the linear models for the former and a lower gain for the latter.

Fig. 9 shows the transferability of the linear models generated for one image (y-axis) to all the other images (x-axis) for the three best performing SOC spectral features showing the  $R^2$  value. For all spectral features the models built for the images A and B (August 2020) were transferable between each other and still led to high accuracies. But these two models could generally not be applied to the other images. The model built on image C could also be applied to image A and E (bare soil composite) for SOC1 and SOC5 with a medium accuracy and vice versa the model built on image E could be applied to the images A and C, too. For image D none of the models performed well, but the model generated for image D and SOC2 showed a medium accuracy when applied to image C.

#### Approaches (b)–(c): Two-step local PLSR and traditional approach

The two-step local PLSR approach (b) consists of a laboratory (first step) as well as a spaceborne model (second step). The results of the laboratory models show high accuracies for image (A)–(C) and the synthetical bare soil image (E) with  $R^2$  values of 0.84–0.86, RMSE

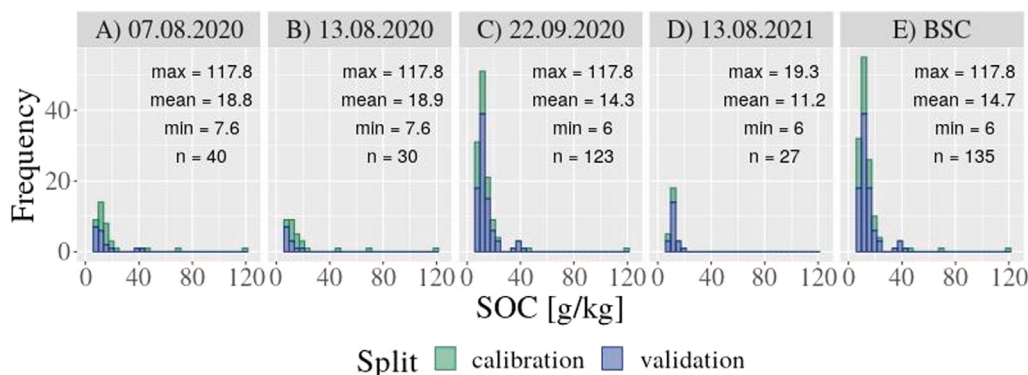


**Fig. 6.** Histograms showing the distributions of SOC contents in the calibration and validation splits for all four images and the multitemporal image (E) BSC = bare soil composite image (workflow one). Minimum, mean and maximum for each dataset in g/kg as well as the number of samples including calibration and validation datasets.

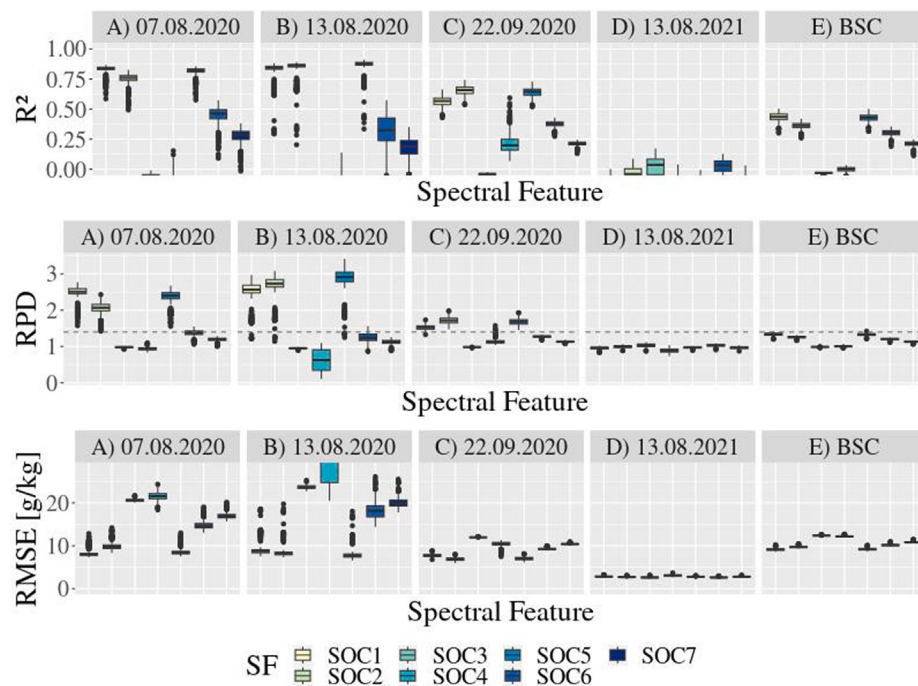


**Fig. 7.**  $R^2$ , RPD and RMSE of all SOC spectral features, approach (a), for the four PRISMA images and the bare soil composite image (workflow one). A repeated random 5-fold cross validation was performed, which leads to slightly variable results. The dashed line in the RPD plot represents RPD = 1.4. The range of the  $R^2$  plot is limited to 0–1 and for the RMSE plot the maximum y-limit is set to 28 g/kg for better visibility.

values of 7.7–10.2 g/kg and RPD > 2.5. For image D no valid laboratory model could be generated. In Fig. 10 measured versus predicted SOC contents are depicted showing the validation split for the two-step local PLSR (b) and the traditional approach (c). Image B shows wide confidence intervals especially for the two-step local PLSR compared to the other images. In general, similar results were observed for both approaches (b) and (c) with a slight tendency of underestimation for approach (b).

#### Approach (d): Traditional with CV

Using the traditional approach with the repeated random cross validation the best results led to high accuracies for all four images with RPD > 2. Only for the bare soil composite (image E) it led to medium results with RPD > 1.5. Fig. 11 shows the variable importance plot for the PLSR cross validation results of the traditional approach (d). Except for the model of image (D) there are multiple important wavelengths with VIP > 1 in all domains of the spectrum. In image (D) the wavelength around 500 nm are the most important.

#### 3.2. Bare soil composite vs. SOC maps composite

In order to combine the four images into one SOC map composite, two workflows were tested and compared. To obtain the comparability of the two workflows, the results of all four images were used as input for workflow two, the SOC maps composite, even if the results for some approaches of single images were low. Nevertheless, the results shown in Table 2 reveal that this workflow two is superior to workflow one, the bare soil composite. Regarding the traditional approach (c) both workflows show similar results. For all other approaches the SOC map composite (workflow two) provides higher accuracies. Especially the SOC spectral feature approach (a) leads to the overall best result in the multitemporal composites using the SOC maps composite with  $R^2 = 0.83$  and RPD = 2.42.

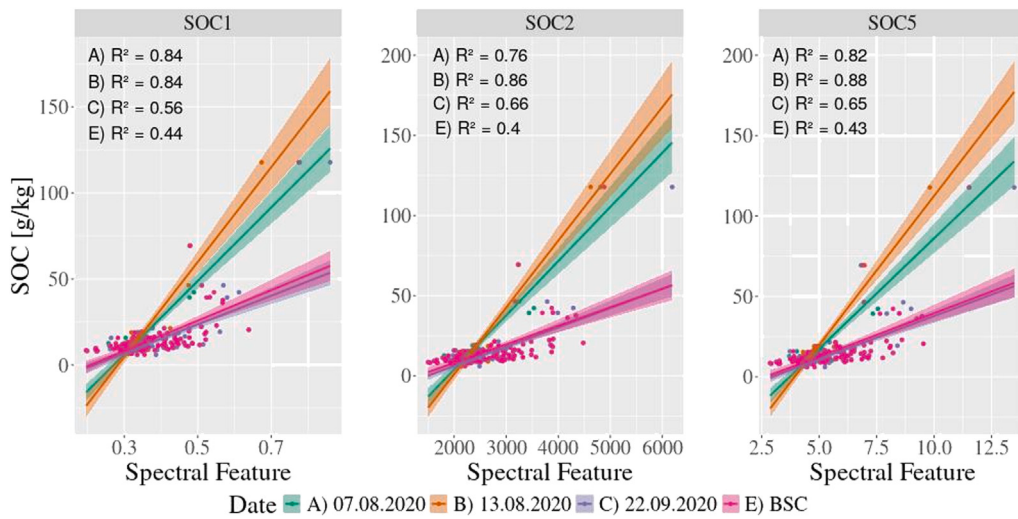


**Fig. 8.** Three SOC spectral feature approaches (approach (a)) versus the measured SOC content. Colored lines are the linear regression line for each date and the BSC = bare soil composite image (workflow one). Shaded areas are the 95% confidence intervals.  $R^2$  values are given for each image and the corresponding spectral feature approach.

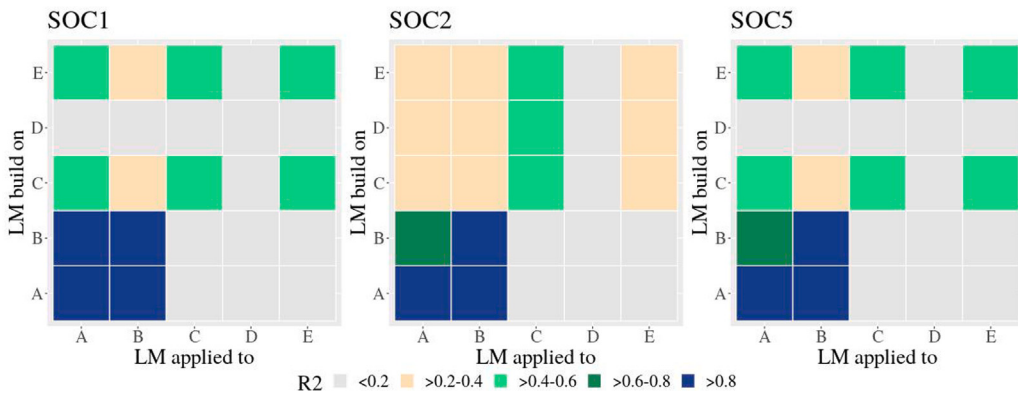


**Fig. 9.** Heatmaps showing the transferability of the linear models (LM) of the best three SOC spectral features, approach (a), to all other images. Shown is the coefficient of determination  $R^2$ . A = 07.08.2020, B = 13.08.2020, C = 22.09.2020, D = 13.08.2021, E = bare soil composite image (workflow one).

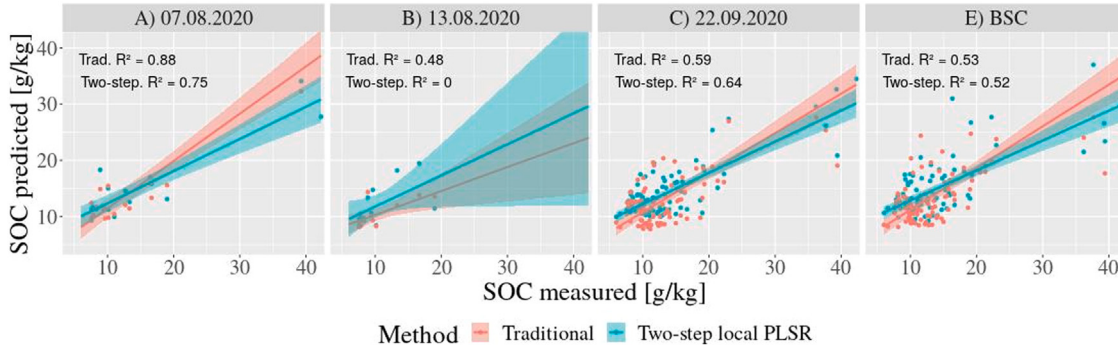


**Fig. 10.** Measured vs. predicted SOC contents showing the validation samples for the best performing approaches of (b) two-step local PLSR and (c) the traditional approach and their coefficients of determination  $R^2$ . Shaded areas are the 95% confidence intervals. Image E is the bare soil composite (workflow one). Results of image (D) are not shown because no valid model could be calibrated for approach (b).

### 3.3. Resulting SOC maps

Fig. 12 (top left) shows the resulting multitemporal SOC map for workflow two, the SOC maps composite (F), and the traditional approach (d) using cross validation. The gray background color represents non-bare soil surfaces and is a gray-scale one band visualization. The SOC map was not cut at the edges and therefore, the slightly spatially differing frames of the single PRISMA images are visible. The spatial

differences originate from differing observation angles during the acquisitions. Fig. 12 (top right) represents a zoom to field scale with the village of Borrentin in its center and reveals more spatial details. The prominent area with high SOC contents, which is located in the image's center is located at the border of a kettle hole.

The second row of Fig. 12 refers to the available number of bare soil scenes per pixel. For about 10% of the pixels in the image one and for

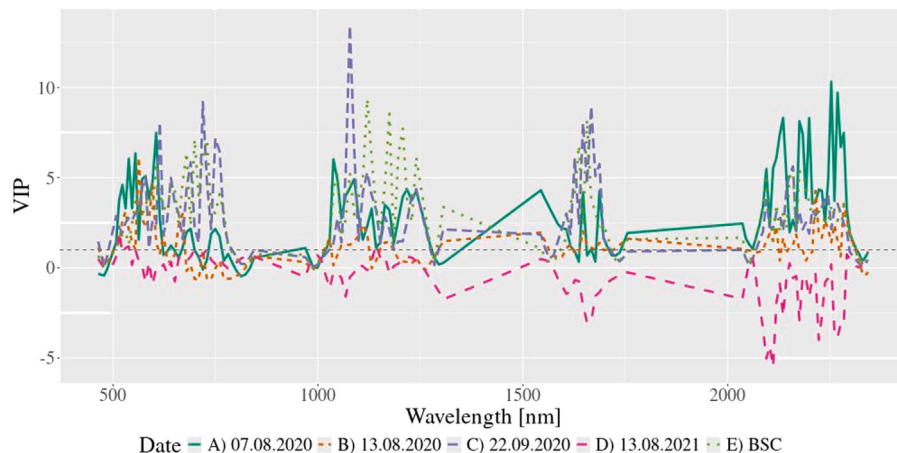


**Fig. 11.** Variable Importance Plot (VIP) for the PLSR cross validation models, approach (d), color coded for the four dates and the BSC = bare soil composite (workflow one). The horizontal dashed gray line is VIP = 1.

**Table 2**

Table showing the best results the two multitemporal workflows using either the bare soil composite (E) or the SOC maps composite (F). RMSE in g/kg. n = number of samples (calibrations resp. validation split or total number of samples if CV is applied). For the SOC maps composite different methods can be used to generate maps for each of the four images separately which is represented in the column "Method".

Date	Approach	Method	R <sup>2</sup>	RPD	RPIQ	RMSE	Bias	n
(E) Bare soil composite	(a)	SOC1 log(SOC)	0.51	1.43	0.66	8.58	1.08	135
	(b)	PLSR	0.52	1.45	1.10	4.93	1.04	46/89
	(c)	GPR	0.53	1.47	1.11	4.86	0.20	46/89
	(d)	PLSR	0.60	1.58	0.73	7.75	-1.12	135
(F) SOC maps composite	(a)	SOC1,2,3,5	0.83	2.42	1.11	5.06	1.92	135
	(b)	PLSR,GPR	0.56	1.51	1.14	4.75	-0.51	46/89
	(c)	PLSR,GPR	0.53	1.47	1.11	4.86	0.52	46/89
	(d)	PLSR	0.79	2.21	1.02	5.55	-0.63	135

Approaches: (a) = SOC spectral feature approach, (b) = two-step local PLSR, (c) = traditional approach with data split into calibration/validation, (d) traditional approach with cross validation.

**Table 3**

Table showing the best results for all approaches for the four dates (A–D). RMSE in g/kg. n = number of samples (calibrations resp. validation split or total number of samples if CV is applied).

Date	Approach	Method	R <sup>2</sup>	RPD	RPIQ	RMSE	Bias	n
(A) 07.08.2020	(a)	SOC1	0.87	2.77	0.92	7.29	-0.04	40
	(b)	PLSR	0.75	2.04	1.44	5.01	0.50	22/18
	(c)	PLSR	0.88	3.02	2.13	3.38	0.77	22/18
	(d)	PLSR	0.90	3.18	1.05	6.35	0.18	40
(B) 13.08.2020	(a)	SOC5	0.91	3.42	1.13	6.58	-0.09	30
	(b)	GPR	0.00	1.05	0.85	3.63	1.54	18/12
	(c)	GPR	0.48	1.44	1.18	2.63	0.00	18/12
	(d)	PLSR	0.90	3.20	1.06	7.03	-1.99	30
(C) 22.09.2020	(a)	SOC2 log(SOC)	0.74	1.98	0.95	5.96	0.70	123
	(b)	GPR	0.64	1.67	1.22	4.35	0.51	37/86
	(c)	GPR	0.59	1.57	1.15	4.63	-0.35	37/86
	(d)	PLSR	0.76	2.06	0.99	5.73	-0.95	123
(D) 13.08.2021	(a)	SOC3	0.17	1.12	0.75	2.43	-0.42	27
	(b)	none	NA	NA	NA	NA	NA	6/21
	(c)	GPR	0.00	1.00	0.77	3.01	-1.20	6/21
	(d)	PLSR	0.81	2.36	1.59	1.15	-0.08	27

Approaches: (a) = SOC spectral feature approach, (b) = two-step local PLSR, (c) = traditional approach with data split into calibration/validation, (d) traditional approach with cross validation.

ca. 8% of the pixels two bare soil scenes were available. The frequency of three or four is more rare, corresponding to 3% and 0.6%.

The third row of Fig. 12 shows the standard deviation (SD) for all pixels with at least one bare soil scene. It was based on the repeated random 5-fold cross validation of the traditional approach (d). As the CV was repeated 100 times for each image it led to 100 to 400 predicted SOC values per pixel. Relative to all pixels with SOC estimations 47% show an SD < 1 g/kg and 86% and SD < 4 g/kg, while 2.6% of the pixels show a higher SD than 17 g/kg.

#### 4. Discussion

**SOC spectral feature approach (a).** Three out of the seven SOC spectral features tested in this study performed well and accuracies were in the same range as for the other approaches. All three spectral features use the visible part of the spectrum from 460–700 nm. This indicates that using spectral features could be a simple and therefore, probably more robust method for estimating the SOC content. Furthermore, estimating a universal link between a SOC spectral feature and the measured SOC content could tremendously ease SOC mapping since

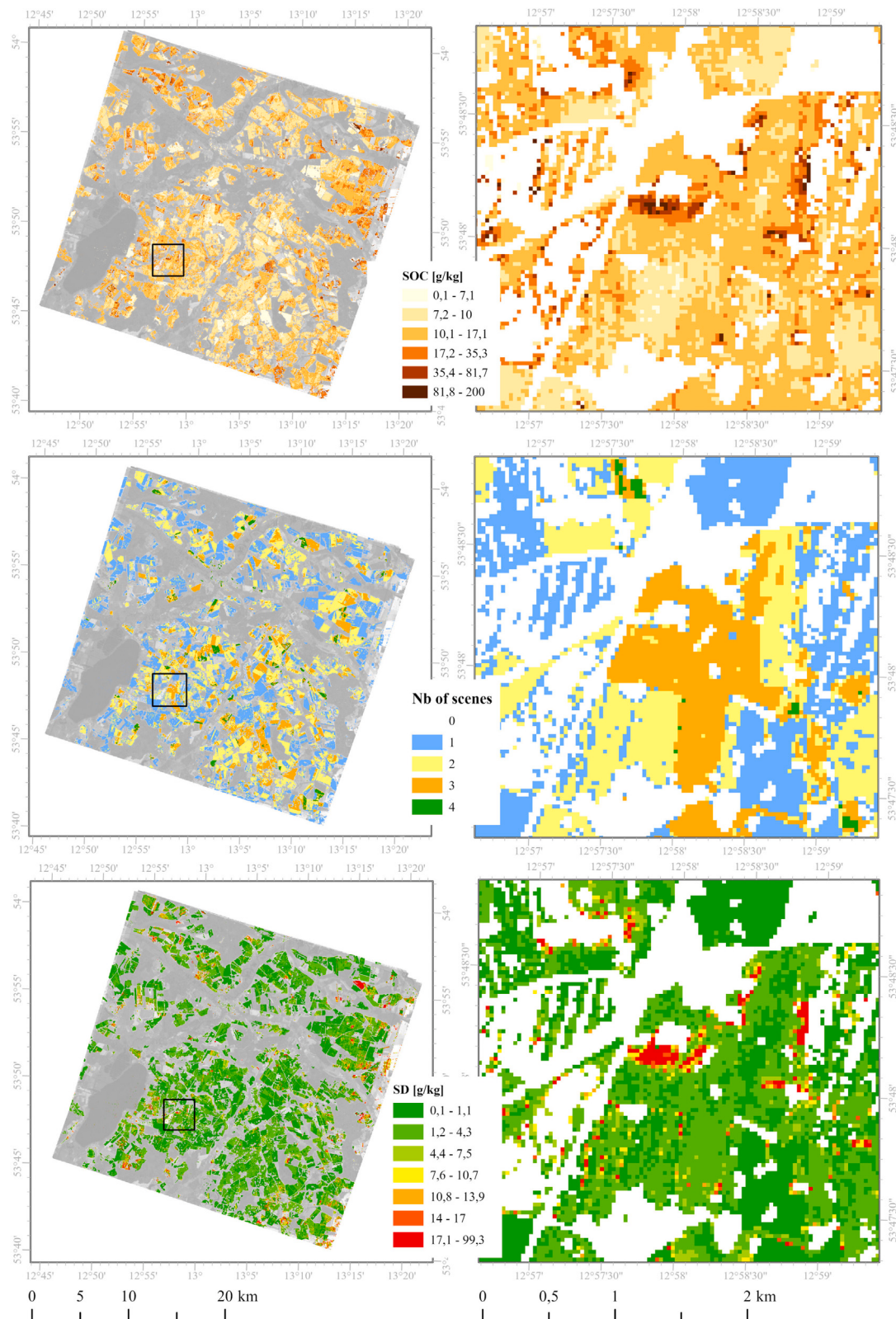


**Fig. 12.** Maps for the whole PRISMA tile (left) and zoom into the area around the village of Borrentin (right). First row: multitemporal SOC maps composite (Image F, approach (d)) showing predicted SOC values. Second row: number of available bare soil scenes per pixel. Third row: Standard deviation of the predicted SOC content for each pixel. Please note that each PRISMA image has a slightly different footprint due to varying observation angles and orbits.

no more calibration samples would be necessary. This study shows that some regression models were transferable to another images but high accuracies could only be maintained if the temporal difference

in between the images was small (e.g. images (A) and (B) with six days) and hence the environmental parameters (e.g. atmospheric and illumination conditions, soil crusts, crop residues) remained similar.

But the transferability to image (C), recorded slightly more than a month later, was already not given anymore. The other way round, the model built on image (C) was transferable to image (A) with medium accuracy. A transferability to another year was only possible in one case. When using SOC2, the model built on image (D) was transferable to image (C) with a medium accuracy.

*Comparison of approaches (b) two-step local PLSR and (c) traditional with data split into cal/val.* To assess the inaccuracy added by using estimated SOC contents based on laboratory models in approach (b), it is compared to approach (c) using traditionally measured SOC contents on the same data splits. Approach (b) shows a moderate decrease in accuracy relative to approach (c) for image (A). But for image (C) this relation is reversed which emphasizes that approach (b) does not always decrease but can also contribute to an increase in accuracy. For the multitemporal approaches the difference between approach (b) and (c) was small. For image (B) the approach (b) was not successful which might be partially explained by a not ideal data split for this image with a comparably low maximum SOC value in the validation subset of <20 g/kg. This assumption is further underlined by the medium high prediction accuracy of approach (c) for this image (B). Due to the conducted laboratory spectroscopy measurements, the calibration samples were already pre-defined before the match ups with the image data and could not be changed. This explanation is further supported by very high accuracies for image (B) using the approaches with cross validation (traditional and SOC spectral features).

*Environmental conditions of the test site.* The terrain of the study area ranges from flat to undulated at field scale. In the latter case, SOC is washed out at the hill tops and accumulates at the depressions which results in a high variability at small scales. Such an area is depicted in Fig. 12 (right). This area was formed by the last ice age and some relicts are the kettle wholes present within many fields. They are small depressions and sometimes filled with water and dense vegetation. This serves as an explanation for the numerous round, oval and longish parts excluded during the bare soil masking step. Additionally, parts within the fields were excluded in cases of moist soils or the presence of too much dry or green vegetation. Furthermore, roads and areas of settlements have been masked as non-soils. In some cases artificial materials with spectral responses similar to soils, e.g. roof tiles have been misclassified as soils.

*SOC maps.* In this study, we applied two workflows and the second workflow of SOC maps compositing proved to be more accurate, although computationally more extensive. This is explainable, since each SOC model is applied on real signal data and can be adapted to the specific environmental conditions. The strength of the bare soil composite (workflow one) is that more samples fall into bare soil pixels for model generation and validation, compared to the SOC maps composite, where usually less samples are available per single image. In the final SOC map (Fig. 12, left) higher SOC concentrations can be found in the north eastern part of the footprint with clay sand soils (1), as well as e.g. in north western part close to the river beds. The zoom (right) compares well to previous work conducted in the same area (Blasch et al., 2015; Castaldi et al., 2019; Ward et al., 2020a). The number of available scenes per pixel does not seem to have an large effect on the uncertainty map. Unlike in Dvorakova et al. (2023) who experienced a higher uncertainty for pixels with few scenes available using up to 24 multispectral Sentinel-2 images. The highest prediction uncertainties are often revealed in areas with the highest SOC contents. These less reliable predictions could partly be induced by the skewed SOC distribution of the ground reference samples with an under representation of high SOC values. Additionally, the pixels in these areas often seem to be influenced by mixed pixel effects, either within fields that still or again contain vegetation or at the field's borders. Dvorakova et al. (2023) also experienced higher SOC values and uncertainties at the borders of the fields caused by mixed pixels.

*Relevance for carbon mapping and monitoring.* Using the multitemporal SOC maps composite approach (workflow two) led to an RMSE of about 5 g/kg or 0.5%. The RMSE is always dependent on the local data range which is wide in this study with up to 120 g/kg leading to higher RMSE values. The accuracy of our approach is in the same range as the annual increase rate which averages to 0.4% and can go up to 8% (Soussana et al., 2019). The previously published studies summarized in Table 1 have less wide SOC ranges and RMSE values ranging between 0.17–0.34%. Thus, monitoring changes of SOC content in the uppermost soil layer over a few years can currently be theoretically possible. Today, it is still limited by the availability of spaceborne imaging spectroscopy data and especially of longer time-series.

*Limitations.* In general, the availability of up-to-date local ground reference databases is a limiting factor due to high costs especially of wet-chemistry analyses. In this study models were built with a lower number of samples, except for image (C), due to reduced availability. Nevertheless, high to very high accuracies were reached in this study for the single images and the two traditional approaches (when excluding image (D)) with an  $R^2$  of 0.48–0.88 for approach (c) (with fixed data split) and 0.76–0.90 for approach (d) (using cross-validation). These results are comparable to the few other satellite based studies that reach  $R^2$  values of 0.64–0.85 using PRISMA and 0.76–0.86 using GaoFen-5 (Gasmi et al., 2022; Mzid et al., 2022; Angelopoulou et al., 2023; Salani et al., 2023; Meng et al., 2020, 2021, 2022; Bao et al., 2021).

Since soils are expected not to change rapidly in this region under constant management practices, the local reference database could be built over several years and is expected to be usable for images acquired a few years later. Unlike for monitoring purposes in the future, where the local reference database should only contain samples with a sampling date close to the observed range for more accurate results. Comparing temporal variations in LUCAS soil sampling points around the study area between 2009 and 2018 demonstrated that the cropland points varied up to 2 g/kg, which is below the uncertainty measures of the prediction.

Despite the temporal gap of three to eight years between the ground reference data and the spaceborne imaging spectroscopy data, most results show high accuracies. This is additionally influenced by the still relatively sparse availability of spaceborne hyperspectral imagery which is further restricted due to cloudiness at the study site and the need for bare soils at the surface. Especially, the availability of multitemporal datasets is currently limited due to the relatively short observation period of the new sensors and their limited acquisition capacity.

In this paper a relatively less strict NDVI threshold of 0.3 was used since at the end of the vegetation period in late summer green photosynthetically active vegetation (PV) is either present (before harvest) or absent (after harvest). As compared to PV, dry non-photosynthetically active vegetation (NPV) is a more critical issue during the times of image acquisitions as spectral signatures of bare soils and NPV are very similar. For this, a more strict nCAI index of 0.014 was chosen to exclude all pixels affected by dry vegetation.

In image (D) acquired in August 2021 only a low number of local ground reference samples match up with bare soil pixels due to PV and a lot of NPV. This image also has an extra year of time lag to the ground reference samples which increases the uncertainty involved. Based on local weather stations, there was precipitation prior to this acquisition date leading to more moist soils compared to the other dates which fall into dry periods. Especially those soil samples with a high SOC content were not part of the bare soil dataset but which seem to be necessary for model calibration. None of the SOC spectral features could be applied and the dataset was too small for a split into calibration and validation subsets. Only for the traditional approach (d) using cross validation good results could be achieved. Nevertheless, the spectra of image (D) were included in the bare soil composite (workflow one) because the spatial coverage of the SOC map benefited since it was the only one

available from another year. For reasons of comparability to workflow one, image (D) was also included in the SOC maps composite (workflow two). The good accuracies of the results, especially of workflow two, show that the median seems to be a robust measure for SOC map compositing.

**Outlook.** The availability of data from spaceborne imaging spectroscopy sensors is growing but still the current missions have limited acquisition capacities that do not allow for a frequent global coverage. This will change in the future with more sensors in orbit including the next generation (e.g. CHIME and SBG) with their wider swaths and regular multitemporal coverage. At the moment, the available data can be used for regional studies in order to find best practices. This study shows all its significance as it demonstrated for the first time new multitemporal SOC map compositing approaches. In this imaging spectroscopy approach the separation of bare soil pixels from other land cover types can be done based on a single image and does not require time-series data. Compared to previous multitemporal multispectral approaches which need the time-series data also for land cover classification in order to identify bare soils. Future studies could focus on optimizing the multitemporal approach in order to use the best signal per pixel and also consider denser multitemporal series whenever possible. Furthermore, the size of a satellite tile is larger compared to airborne campaigns and this opens up the perspective of large scale soil property mapping and monitoring. In this context the model's spatial borders of validity to e.g. one or more tiles should be evaluated.

## 5. Conclusion

In order to test and improve the mapping situation for soil organic carbon (SOC) in top-soils, best practices should be found for retrieving the SOC content using the recently launched, spaceborne imaging spectroscopy sensors of the latest generation. Four imaging spectroscopy tiles with the same footprint recorded by the PRISMA sensor were used over a study site in northern Germany. Different SOC modeling approaches were tested: In approach (a) three out of seven tested SOC spectral features using the visible part of the spectrum performed well for most images. The linear regression models in this approach were transferable to another PRISMA image with high accuracies if the acquisition dates had a small temporal difference of a few days. Approach (b) was a two-step local PLSR approach which used laboratory spectra from the local ground reference database and the European scale LUCAS Soil database to model the SOC contents and thereby replaced wet-chemistry analyses. It revealed mostly similar accuracies compared to (c) the traditional approach based on measured SOC contents and the same data split. Best results for the single images were achieved when using approach (d) the traditional approach with cross validation with an  $R^2$  of 0.76–0.90 and a RPD of 2.06–3.20. Furthermore, two different workflows were compared that combine the four images into one multitemporal SOC composite map. Merging the SOC maps of the single images using the median (workflow two) was better than estimating the SOC content with a model based on a synthetical bare soil multitemporal composite (workflow one). The overall best multitemporal results were generated using the SOC spectral feature approach (a) in workflow two with  $R^2 = 0.83$  and RPD = 2.42. Nevertheless, the final SOC map was based on the traditional PLSR approach which was more robust for all input dates and reached similar accuracies ( $R^2 = 0.79$  and RPD = 2.21). Creating a separate model for each date to produce individual SOC maps and to merge them in the end seemed to cope better with changing environmental variables and it allowed the SOC models to be run on real satellite signals. Since the imaging spectroscopy sensors of the latest generation have just recently been launched, this study provides a first step towards the evaluation of the potential and examination of methods for generating temporal composites. In the future with more imaging spectroscopy sensors in orbit a higher temporal coverage of the agricultural areas

will be realized. This opens up new perspectives for large scale SOC mapping and monitoring. New challenges will need to be addressed considering adequate local ground reference data, model transferability and multitemporal approaches.

## Funding

This research was funded within the EnMAP science program under the German Space Agency at DLR with resources from the German Federal Ministry for Economic Affairs and Climate Action, grant number 50EE1923.

## CRediT authorship contribution statement

**Kathrin J. Ward:** Writing – review & editing, Writing – original draft, Visualization, Validation, Software, Methodology, Investigation, Formal analysis, Data curation, Conceptualization. **Saskia Foerster:** Writing – review & editing, Supervision, Resources, Funding acquisition, Conceptualization. **Sabine Chabrillat:** Writing – review & editing, Supervision, Resources, Project administration, Funding acquisition, Conceptualization.

## Declaration of competing interest

The authors declare that they have no known competing financial interests or personal relationships that could have appeared to influence the work reported in this paper.

## Data availability

Data will be made available on request.

## Acknowledgments

The authors wish to thank Ettore Lopinto and Giovanni Rum (ASI), and Marco Celesti (ESA) for the provision of the PRISMA images under the CHIME HYPERSENSE sites monitoring program. PRISMA products were generated by K.J. Ward under an ASI License to Use; Original PRISMA Product - ©ASI - (2020, 2021). The LUCAS Soil dataset which was made available by the European Commission through the European Soil Data Centre managed by the Joint Research Centre (JRC) (<http://esdac.jrc.ec.europa.eu/>).

We would like to thank Carsten Neumann for providing a template of an R script on Savitzky–Golay smoothing for spectra with excluded water bands. We thank Gerald Blasch for providing soil samples collected in 2013. Furthermore, we thank Marco Bravin (UCLouvain) and Michael Facklam for the essential soil organic carbon measurements, the laboratories of the REQUASUD agricultural extension service network for soil spectral laboratory measurements.

## References

- Alonso, K., Bachmann, M., Burch, K., Carmona, E., Cerra, D., De los Reyes, R., Dietrich, D., Heiden, U., Hölderlin, A., Ickes, J., et al., 2019. Data products, quality and validation of the DLR earth sensing imaging spectrometer (DESI). Sensors 19 (20), 4471.
- Angelopoulou, T., Chabrillat, S., Pignatti, S., Milewski, R., Karyotis, K., Brell, M., Ruhtz, T., Bochtis, D., Zalidis, G., 2023. Evaluation of airborne hyperspectral remote sensing data for soil organic matter and carbonates estimation. Remote Sens. 15 (4), 1106.
- Bao, Y., Ustin, S., Meng, X., Zhang, X., Guan, H., Qi, B., Liu, H., 2021. A regional-scale hyperspectral prediction model of soil organic carbon considering geomorphic features. Geoderma 403, 115263.
- Barnsley, M.J., Settle, J.J., Cutler, M.A., Lobb, D.R., Teston, F., 2004. The PROBA/CHRIS mission: A low-cost smallsat for hyperspectral multiangle observations of the earth surface and atmosphere. IEEE Trans. Geosci. Remote Sens. 42 (7), 1512–1520.
- Bartholomew, H., Schaeppman, M.E., Kooistra, L., Stevens, A., Hoogmoed, W., Spaargaren, O., 2008. Spectral reflectance based indices for soil organic carbon quantification. Geoderma 145 (1–2), 28–36.

- Ben-Dor, E., Chabrillat, S., Dematté, J.A.M., Taylor, G., Hill, J., Whiting, M., Sommer, S., 2009. Using imaging spectroscopy to study soil properties. *Remote Sens. Environ.* 113, S38–S55.
- Ben-Dor, E., Inbar, Y., Chen, Y., 1997. The reflectance spectra of organic matter in the visible near-infrared and short wave infrared region (400–2500 nm) during a controlled decomposition process. *Remote Sens. Environ.* 61 (1), 1–15.
- Ben-Dor, E., Taylor, R., Hill, J., Dematté, J.A.M., Whiting, M., Chabrillat, S., Sommer, S., 2008. Imaging spectrometry for soil applications. *Adv. Agron.* 97, 321–392.
- Beyer, L., Kahle, P., Kretschmer, H., Wu, Q., 2001. Soil organic matter composition of man-impacted urban sites in north Germany. *J. Plant Nutr. Soil Sci.* 164 (4), 359–364.
- BGR, 2007. Karte der Bodenarten in Oberböden 1:1.000.000 (BOART1000OB), Version 2.0. Bundesanstalt für Geowissenschaften und Rohstoffe (BGR) Hannover, Germany.
- BGR, 2013. Soil map of the federal Republic of Germany 1:1,000,000 (BUEK1000en), version 2.1. Bundesanstalt für Geowissenschaften und Rohstoffe (BGR) Hannover, Germany.
- Blasch, G., Spengler, D., Itzert, S., Wessolek, G., 2015. Organic matter modeling at the landscape scale based on multitemporal soil pattern analysis using RapidEye data. *Remote Sens.* 7 (9), 11125–11150.
- Breiman, L., 2001. Random forests. *Mach. Learn.* 45, 5–32.
- Castaldi, F., Chabrillat, S., Jones, A., Vreys, K., Bomans, B., Van Wesemael, B., 2018. Soil organic carbon estimation in croplands by hyperspectral remote APEX data using the LUCAS topsoil database. *Remote Sens.* 10 (2), 153.
- Castaldi, F., Chabrillat, S., van Wesemael, B., 2019. Sampling strategies for soil property mapping using multispectral sentinel-2 and hyperspectral EnMAP satellite data. *Remote Sens.* 11 (3), 309.
- Castaldi, F., Koparan, M.H., Wetterlind, J., Žydelis, R., Vinci, I., Savaş, A.Ö., Kivrak, C., Tunçay, T., Volungevičius, J., Obber, S., et al., 2023. Assessing the capability of sentinel-2 time-series to estimate soil organic carbon and clay content at local scale in croplands. *ISPRS J. Photogramm. Remote Sens.* 199, 40–60.
- Cawse-Nicholson, K., Townsend, P.A., Schimel, D., Assiri, A.M., Blake, P.L., Buongiorno, M.F., Campbell, P., Carmon, N., Casey, K.A., Correa-Pabón, R.E., et al., 2021. NASA's surface biology and geology designated observable: A perspective on surface imaging algorithms. *Remote Sens. Environ.* 257, 112349.
- Chabrillat, S., Ben-Dor, E., Cierniewski, J., Gomez, C., Schmid, T., van Wesemael, B., 2019. Imaging spectroscopy for soil mapping and monitoring. *Surv. Geophys.* 40, 361–399.
- Chabrillat, S., Eisele, A., Guillaso, S., Rogäß, C., Ben-Dor, E., Kaufmann, H., 2011. HYSOMA: An easy-to-use software interface for soil mapping applications of hyperspectral imagery. In: Proceedings of the 7th EARSeL SIG Imaging Spectroscopy Workshop. Edinburgh, UK, pp. 11–13.
- Chabrillat, S., Guillaso, S., Rabe, A., Foerster, S., Guanter, L., 2016. From HYSOMA to ENSMAP - a new open source tool for quantitative soil properties mapping based on hyperspectral imagery from airborne to spaceborne applications. In: EGU General Assembly Conference Abstracts. pp. EPSC2016–14697.
- Cogliati, S., Sarti, F., Chiarantini, L., Cosi, M., Lorusso, R., Lopinto, E., Miglietta, F., Genesio, L., Guanter, L., Damm, A., et al., 2021. The PRISMA imaging spectroscopy mission: Overview and first performance analysis. *Remote Sens. Environ.* 262, 112499.
- De Rosa, D., Ballabio, C., Lugato, E., Fasiolo, M., Jones, A., Panagos, P., 2024. Soil organic carbon stocks in European croplands and grasslands: How much have we lost in the past decade? *Global Change Biol.* 30 (1), e16992.
- Díaz-Uriarte, R., Alvarez de Andrés, S., 2006. Gene selection and classification of microarray data using random forest. *BMC Bioinform.* 7, 1–13.
- Dvorakova, K., Heiden, U., Pepers, K., Staats, G., van Os, G., van Wesemael, B., 2023. Improving soil organic carbon predictions from a sentinel-2 soil composite by assessing surface conditions and uncertainties. *Geoderma* 429, 116128.
- Folkman, M.A., Pearlman, J., Liao, L.B., Jarecke, P.J., 2001. EO-1/Hyperion hyperspectral imager design, development, characterization, and calibration. *Hyperspectr. Remote Sens. Land Atmos.* 4151, 40–51.
- Frazier, B., Cheng, Y., 1989. Remote sensing of soils in the eastern palouse region with landsat thematic mapper. *Remote Sens. Environ.* 28, 317–325.
- Gasmi, A., Gomez, C., Chehbouni, A., Dhiba, D., El Gharous, M., 2022. Using PRISMA hyperspectral satellite imagery and GIS approaches for soil fertility mapping (FertiMap) in Northern Morocco. *Remote Sens.* 14 (16), 4080.
- Genot, V., Colinet, G., Bock, L., Vanvyve, D., Reusen, Y., Dardenne, P., 2011. Near infrared reflectance spectroscopy for estimating soil characteristics valuable in the diagnosis of soil fertility. *J. Near Infrared Spectrosc.* 19 (2), 117–138.
- Gerighausen, H., Menz, G., Kaufmann, H., et al., 2012. Spatially explicit estimation of clay and organic carbon content in agricultural soils using multi-annual imaging spectroscopy data. *Appl. Environ. Soil Sci.* 2012.
- Gomez, C., Rossel, R.A.V., McBratney, A.B., 2008. Soil organic carbon prediction by hyperspectral remote sensing and field vis-NIR spectroscopy: An Australian case study. *Geoderma* 146 (3–4), 403–411.
- Green, R.O., Mahowald, N., Thompson, D.R., Ung, C., Brodrick, P., Pollock, R., Bennett, M., Lundein, S., Joyce, M., Olson-Duvall, W., et al., 2023. Performance and early results from the earth surface mineral dust source investigation (EMIT) imaging spectroscopy mission. In: 2023 IEEE Aerospace Conference. IEEE, pp. 1–10.
- Haubrock, S.-N., Chabrillat, S., Lemmnitz, C., Kaufmann, H., 2008. Surface soil moisture quantification models from reflectance data under field conditions. *Int. J. Remote Sens.* 29 (1), 3–29.
- He, T., Wang, J., Lin, Z., Cheng, Y., 2009. Spectral features of soil organic matter. *Geo-spat. Inf. Sci.* 12 (1), 33–40.
- Hijmans, R.J., 2021. Terra: Spatial data analysis. URL <https://CRAN.R-project.org/package=terra>, R package version 1.4-22.
- Hijmans, R.J., van Etten, J., 2012. Raster: Geographic analysis and modeling with raster data. URL <https://CRAN.R-project.org/package=raster>, R package version 2.0-12.
- Karatzoglou, A., Smola, A., Hornik, K., 2022. Kernlab: Kernel-based machine learning lab. URL <https://CRAN.R-project.org/package=kernlab>, R package version 0.9-31.
- Karatzoglou, A., Smola, A., Hornik, K., Zeileis, A., 2004. Kernlab – An S4 package for kernel methods in R. *J. Stat. Softw.* 11 (9), 1–20. <http://dx.doi.org/10.18637/jss.v011.i09>.
- Liaw, A., Wiener, M., 2002. Classification and regression by randomforest. *R News* 2 (3), 18–22, URL <https://CRAN.R-project.org/doc/Rnews/>.
- Liland, K.H., rn Helge Mevik, B., Wehrens, R., 2021. Pls: Partial least squares and principal component regression. URL <https://CRAN.R-project.org/package=pls>, R package version 2.8-0.
- Liu, Y.-N., Sun, D.-X., Hu, X.-N., Ye, X., Li, Y.-D., Liu, S.-F., Cao, K.-Q., Chai, M.-Y., Zhang, J., Zhang, Y., et al., 2019. The advanced hyperspectral imager: aboard China's gaofen-5 satellite. *IEEE Geosci. Remote Sens. Mag.* 7 (4), 23–32.
- Martens, H., Naes, T., 1989. Multivariate Calibration. John Wiley and Sons Ltd, Chichester, UK.
- Meng, X., Bao, Y., Liu, J., Liu, H., Zhang, X., Zhang, Y., Wang, P., Tang, H., Kong, F., 2020. Regional soil organic carbon prediction model based on a discrete wavelet analysis of hyperspectral satellite data. *Int. J. Appl. Earth Obs. Geoinf.* 89, 102111.
- Meng, X., Bao, Y., Wang, Y., Zhang, X., Liu, H., 2022. An advanced soil organic carbon content prediction model via fused temporal-spatial-spectral (TSS) information based on machine learning and deep learning algorithms. *Remote Sens. Environ.* 280, 113166.
- Meng, X., Bao, Y., Ye, Q., Liu, H., Zhang, X., Tang, H., Zhang, X., 2021. Soil organic matter prediction model with satellite hyperspectral image based on optimized denoising method. *Remote Sens.* 13 (12), 2273.
- Middleton, E.M., Campbell, P.K., Ong, L., Landis, D.R., Zhang, Q., Neigh, C.S., Huemmrich, K.F., Ungar, S.G., Mandl, D.J., Frye, S.W., et al., 2017. Hyperion: The first global orbital spectrometer, earth observing-1 (EO-1) satellite (2000–2017). In: 2017 IEEE International Geoscience and Remote Sensing Symposium. IGARSS, IEEE, pp. 3039–3042.
- Minasny, B., Malone, B.P., McBratney, A.B., Angers, D.A., Arrouays, D., Chambers, A., Chaplot, V., Chen, Z.-S., Cheng, K., Das, B.S., et al., 2017. Soil carbon 4 per mille. *Geoderma* 292, 59–86.
- Mzid, N., Castaldi, F., Tolomio, M., Pascucci, S., Casa, R., Pignatti, S., 2022. Evaluation of agricultural bare soil properties retrieval from landsat 8, sentinel-2 and PRISMA satellite data. *Remote Sens.* 14 (3), 714.
- Nieke, J., Rast, M., 2018. Towards the copernicus hyperspectral imaging mission for the environment (CHIME). In: Igarras 2018–2018 Ieee International Geoscience and Remote Sensing Symposium. IEEE, pp. 157–159.
- Nocita, M., Stevens, A., Toth, G., Panagos, P., van Wesemael, B., Montanarella, L., 2014. Prediction of soil organic carbon content by diffuse reflectance spectroscopy using a local partial least square regression approach. *Soil Biol. Biochem.* 68, 337–347.
- Nocita, M., Stevens, A., van Wesemael, B., Aitkenhead, M., Bachmann, M., Barthès, B., Dor, E.B., Brown, D.J., Clairotte, M., Csorba, A., et al., 2015. Soil spectroscopy: an alternative to wet chemistry for soil monitoring. *Adv. Agron.* 132, 139–159.
- Orgiazzi, A., Ballabio, C., Panagos, P., Jones, A., Fernández-Ugalde, O., 2018. LUCAS soil, the largest expandable soil dataset for europe: a review. *Eur. J. Soil Sci.* 69 (1), 140–153.
- Peón, J., Recondo, C., Fernández, S., F. Calleja, J., De Miguel, E., Carretero, L., 2017. Prediction of topsoil organic carbon using airborne and satellite hyperspectral imagery. *Remote Sens.* 9 (12), 1211.
- Rasmussen, C.E., 2004. Gaussian processes for machine learning. In: Bousquet, O., von Luxburg, U., Rätsch, G. (Eds.), Advanced Lectures on Machine Learning. ML 2003, In: Lecture Notes in Computer Science, vol. 3176, Springer, Heidelberg.
- Salani, G.M., Lissoni, M., Bianchini, G., Brombin, V., Natali, S., Natali, C., 2023. Soil organic carbon estimation in ferrara (northern Italy) combining in situ geochemical analyses and hyperspectral remote sensing. *Environments* 10 (10), 173.
- Scheffler, D., 2017. AROSICS: An Automated and Robust Open-Source Image Co-Registration Software for Multi-Sensor Satellite Data. <http://dx.doi.org/10.5281/zenodo.3743085>, This is the version as used in Scheffler et al. (2017): <http://www.mdpi.com/2072-4292/9/7/676>.
- Scheffler, D., Hollstein, A., Diedrich, H., Segl, K., Hostert, P., 2017. AROSICS: An automated and robust open-source image co-registration software for multi-sensor satellite data. *Remote Sens.* 9 (7), 676.
- signal developers, 2014. signal: Signal processing. URL <http://r-forge.r-project.org/projects/signal/>.
- Soussana, J.-F., Lutfalla, S., Ehrhardt, F., Rosenstock, T., Lamanna, C., Havlík, P., Richards, M., Chotte, J.-L., Torquebiau, E., Ciais, P., et al., 2019. Matching policy and science: Rationale for the '4 per 1000-soils for food security and climate' initiative. *Soil Tillage Res.* 188, 3–15.
- Spengler, D., Foerster, M., Borg, E., 2018. Editorial. *PFG J. Photogr. Remote Sens. Geoinf. Sci.* 86, 49–51.
- Stenberg, B., Rossel, R.A.V., Mouazen, A.M., Wetterlind, J., 2010. Visible and near infrared spectroscopy in soil science. *Adv. Agron.* 107, 163–215.

- Stevens, A., Nocita, M., Tóth, G., Montanarella, L., van Wesemael, B., 2013. Prediction of soil organic carbon at the European scale by visible and near infrared reflectance spectroscopy. *PLoS One* 8 (6), e66409.
- Storch, T., Honold, H.-P., Chabrillat, S., Habermeyer, M., Tucker, P., Brell, M., Ohndorf, A., Wirth, K., Betz, M., Kuchler, M., et al., 2023. The EnMAP imaging spectroscopy mission towards operations. *Remote Sens. Environ.* 294, 113632.
- Thaler, E.A., Larsen, I.J., Yu, Q., 2019. A new index for remote sensing of soil organic carbon based solely on visible wavelengths. *Soil Sci. Soc. Am. J.* 83 (5), 1443–1450.
- Thompson, D.R., Schimel, D.S., Poulter, B., Brosnan, I., Hook, S.J., Green, R.O., Glenn, N., Guild, L., Henn, C., Cawse-Nicholson, K., et al., 2020. NASA's surface biology and geology concept study: Status and next steps. In: IGARSS 2020–2020 IEEE International Geoscience and Remote Sensing Symposium. IEEE, pp. 3269–3271.
- Tóth, G., Hermann, T., da Silva, M.R., Montanarella, L., 2018. Monitoring soil for sustainable development and land degradation neutrality. *Environ. Monit. Assess.* 190, 1–4.
- Toth, G., Jones, A., Montanarella, L., Alewell, C., Ballabio, C., Carre, F., De Brogniez, D., Guicharnaud, R.A., Gardi, C., Hermann, T., et al., 2013. LUCAS Topoil Survey—Methodology, Data and Results. Publications Office of the European Union, JRC Technical Reports; EUR26102-Scientific and Technical Research Series.
- Tziolas, N., Tsakiridis, N., Chabrillat, S., Demattè, J., Ben-Dor, E., Gholizadeh, A., Zalidis, G., Wesemael, B.E.O.D.-D., 2021. Earth observation data-driven cropland soil monitoring: A review. *Remote Sens.* 13, 4439.
- Urai, M., Tsuchida, S., Yamamoto, S., Tachikawa, T., Iwasaki, A., Ishii, J., et al., 2021. Initial onboard calibration results of the HISUI hyperspectral sensor. In: 2021 IEEE International Geoscience and Remote Sensing Symposium IGARSS. IEEE, pp. 1608–1610.
- Vaudour, E., Gholizadeh, A., Castaldi, F., Saberioon, M., Borůvka, L., Urbina-Salazar, D., Fouad, Y., Arrouays, D., Richer-de Forges, A.C., Biney, J., et al., 2022. Satellite imagery to map topsoil organic carbon content over cultivated areas: an overview. *Remote Sens.* 14 (12), 2917.
- Vaudour, E., Gomez, C., Lagacherie, P., Loiseau, T., Baghdadi, N., Urbina-Salazar, D., Loubet, B., Arrouays, D., 2021. Temporal mosaicking approaches of sentinel-2 images for extending topsoil organic carbon content mapping in croplands. *Int. J. Appl. Earth Obs. Geoinf.* 96, 102277.
- Vaudour, E., Gomez, C., Loiseau, T., Baghdadi, N., Loubet, B., Arrouays, D., Ali, L., Lagacherie, P., 2019. The impact of acquisition date on the prediction performance of topsoil organic carbon from sentinel-2 for croplands. *Remote Sens.* 11 (18), 2143.
- Viscarra Rossel, R., Behrens, T., 2010. Using data mining to model and interpret soil diffuse reflectance spectra. *Geoderma* 158 (1–2), 46–54.
- Ward, K.J., Chabrillat, S., Brell, M., Castaldi, F., Spengler, D., Foerster, S., 2020a. Mapping soil organic carbon for airborne and simulated enmap imagery using the LUCAS soil database and a local PLSR. *Remote Sens.* 12 (20), 3451.
- Ward, K.J., Chabrillat, S., Foerster, S., 2020b. LocalplsR. URL <https://github.com/GFZ/LocalPLSR>.
- Ward, K.J., Chabrillat, S., Neumann, C., Foerster, S., 2019. A remote sensing adapted approach for soil organic carbon prediction based on the spectrally clustered LUCAS soil database. *Geoderma* 353, 297–307.
- Wu, M., Dou, S., Lin, N., Jiang, R., Zhu, B., 2023. Estimation and mapping of soil organic matter content using a stacking ensemble learning model based on hyperspectral images. *Remote Sens.* 15 (19), 4713.
- Zacharias, S., Bogena, H., Samaniego, L., Mauder, M., Fuß, R., Puetz, T., Frenzel, M., Schwank, M., Baessler, C., Butterbach-Bahl, K., et al., 2011. A network of terrestrial environmental observatories in Germany. *Vadose Zone J.* 10 (3), 955–973.
- Zepp, S., Heiden, U., Bachmann, M., Wiesmeier, M., Steininger, M., Van Wesemael, B., 2021. Estimation of soil organic carbon contents in croplands of Bavaria from SCMaP soil reflectance composites. *Remote Sens.* 13 (16), 3141.